

Differentiable Rendering with Reparameterized Volume Sampling

Nikita Morozov¹ Denis Rakitin¹ Oleg Desheulin¹ Dmitry Vetrov^{1,2} Kirill Struminsky¹

Abstract

In view synthesis, a neural radiance field approximates underlying density and radiance fields based on a sparse set of scene pictures. To generate a pixel of a novel view, it marches a ray through the pixel and computes a weighted sum of radiance emitted from a dense set of ray points. This rendering algorithm is fully differentiable and facilitates gradient-based optimization of the fields. However, in practice, only a tiny opaque portion of the ray contributes most of the radiance to the sum. We propose an end-to-end differentiable sampling algorithm based on inverse transform sampling. It generates samples according to the probability distribution induced by the density field and picks non-transparent points on the ray. We utilize the algorithm in two ways. First, we propose a novel rendering approach based on Monte Carlo estimates. Such a rendering algorithm allows for optimizing a neural radiance field with just a few radiance field evaluations per ray. Second, we use the sampling algorithm to modify the hierarchical scheme used in the original work on neural radiance fields. In this setup, we were able to train the proposal network end-to-end without any auxiliary losses and improved the baseline performance.

1. Introduction

Recently, learning-based approaches led to significant progress in novel view synthesis. As an early instance, (Mildenhall et al., 2020) represents a scene via a density field and a radiance (color) field parameterized with an MLP. Using a differentiable volume rendering algorithm (Max, 1995) with the MLP-based fields to produce images, they minimize the discrepancy between the output images and a set of reference images to learn a scene

¹HSE University, Moscow, Russia ²AIRI, Moscow, Russia. Correspondence to: Kirill Struminsky <k.struminsky@gmail.com>.

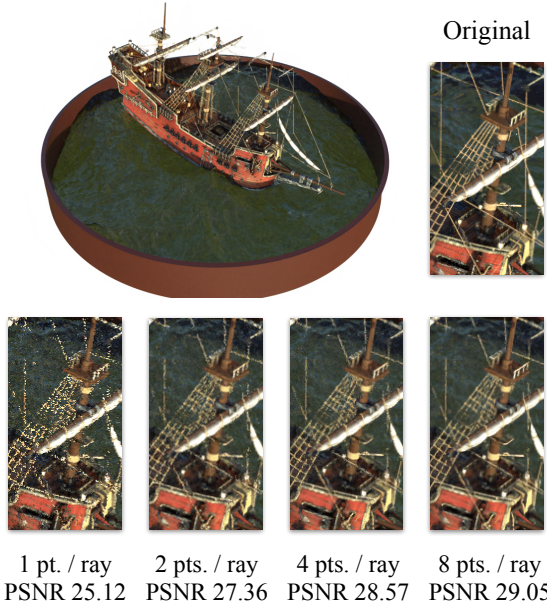


Figure 1: Novel views of a ship generated with the proposed Monte Carlo radiance estimates. For each ray we estimate density and then compute radiance at a few ray points generated using the ray density. As the above images indicate, render quality gradually improves with the number of ray samples without visible artifacts at eight points per ray.

representation.

In particular, NeRF generates an image pixel by casting a ray from a camera through the pixel and aggregating the radiance at each ray point with weights induced by the density field. Each term involves a costly neural network query, and model has a trade-off between rendering quality and computational load. In this work, we revisit the formula for the aggregated radiance computation and propose a novel approximation based on Monte Carlo methods. We compute our approximation in two stages. In the first stage, we march through the ray to estimate density. In the second stage, we construct a Monte Carlo color approximation using the density to pick points along the ray. The resulting estimate is fully-differentiable and can act as a drop-in replacement for the standard rendering algorithm used in NeRF. Fig. 1

illustrates the estimates for a varying number of samples. Compared to the standard rendering algorithm, the second stage of our algorithm avoids redundant radiance queries and can potentially reduce computation during training and inference.

Furthermore, we show that the sampling algorithm used in our Monte Carlo estimate is applicable to the hierarchical sampling scheme in NeRF. Similar to our work, the hierarchical scheme uses inverse transform sampling to pick points along a ray. The corresponding distribution is tuned using an auxiliary training task. In contrast, we derive our algorithm from a different perspective and obtain the inverse transform sampling for a slightly different distribution. With our algorithm, we were able to train NeRF end-to-end without the auxiliary task and improve the reconstruction quality. We achieve this by back-propagating the gradients through the sampler and show that the original sampling algorithm fails to achieve similar quality in the same setup.

Below, Section 2 gives a recap of neural radiance fields. Then we proceed to the main contribution of our work in Section 3, namely the rendering algorithm fueled by Monte Carlo estimates with a novel sampling procedure. In Subsection 5.1, we compare our sampling algorithm against the hierarchical sampling scheme proposed for training NeRF. In Subsection 5.2 we evaluate our Monte Carlo approximation in a one-dimensional setting. Finally, in Subsection 5.3 we apply the proposed Monte Carlo estimate to replace the standard rendering algorithm. With an efficient neural radiance field architecture, our algorithm decreases time per training iteration at the cost of reduced reconstruction quality. Our source code is available at <https://github.com/GreatDrake/reparameterized-volume-sampling>.

2. Neural Radiance Fields

Neural radiance fields represent 3D scenes with a non-negative scalar density field $\sigma : \mathbb{R}^3 \rightarrow \mathbb{R}^+$ and a vector radiance field $c : \mathbb{R}^3 \times \mathbb{R}^3 \rightarrow \mathbb{R}^3$. Scalar field σ represents volume density at each spatial location \mathbf{x} , and $c(\mathbf{x}, \mathbf{d})$ returns the light emitted from spatial location \mathbf{x} in direction \mathbf{d} represented as a normalized three dimensional vector.

For novel view synthesis, NeRF (Mildenhall et al., 2020) adapts a volume rendering algorithm that computes pixel color $C(\mathbf{r})$ as the expected radiance for a ray $\mathbf{r} = \mathbf{o} + t\mathbf{d}$ passing through a pixel from origin $\mathbf{o} \in \mathbb{R}^3$ in a direction $\mathbf{d} \in \mathbb{R}^3$. For ease of notation, we will denote density and radiance restricted to a ray \mathbf{r} as

$$\sigma_{\mathbf{r}}(t) := \sigma(\mathbf{o} + t\mathbf{d}) \text{ and } c_{\mathbf{r}}(t) := c(\mathbf{o} + t\mathbf{d}, \mathbf{d}). \quad (1)$$

With that in mind, the expected radiance along ray \mathbf{r} is given

as

$$C(\mathbf{r}) = \int_{t_n}^{t_f} p_{\mathbf{r}}(t) c_{\mathbf{r}}(t) dt, \quad (2)$$

where

$$p_{\mathbf{r}}(t) := \sigma_{\mathbf{r}}(t) \exp \left(- \int_{t_n}^t \sigma_{\mathbf{r}}(s) ds \right). \quad (3)$$

Here, t_n and t_f are *near* and *far* ray boundaries and $p_{\mathbf{r}}(t)$ is an unnormalized probability density function of a random variable t on a ray \mathbf{r} . Intuitively, t is the location on a ray where the portion of light coming into the point \mathbf{o} was emitted.

To approximate the nested integrals in Eq. 2, (Max, 1995) proposed to replace fields $\sigma_{\mathbf{r}}$ and $c_{\mathbf{r}}$ with a piecewise approximation on a grid $t_n = t_0 < t_1 < \dots < t_m = t_f$ and compute the formula in Eq. 2 analytically for the approximation. In particular, a piecewise constant approximation with denisty σ_i and radiance c_i within i -th bin $[t_{i+1}, t_i]$ of width $\delta_i = t_{i+1} - t_i$ yields formula

$$\hat{C}(\mathbf{r}) = \sum_{i=1}^m w_i c_i, \quad (4)$$

where the weights are given by

$$w_i = (1 - \exp(-\sigma_i \delta_i)) \exp \left(- \sum_{j=1}^{i-1} \sigma_j \delta_j \right). \quad (5)$$

Importantly, Eq. 4 is fully differentiable and can be used as a part of gradient-based learning pipeline. To reconstruct a scene NeRF runs a gradient based optimizer to minimize MSE between the predicted color and the ground truth color averaged across multiple rays and multiple viewpoints.

While the above approximation works in practice, it involves multiple evaluations of c and σ along a dense grid. Besides that, a ray typically intersects a solid surface at some point $t \in [t_n, t_f]$. In this case, probability density $p_{\mathbf{r}}(t)$ will concentrate its mass near t and, as a result, most of the terms in Eq. 4 will make negligible contribution to the sum. To approach this problem, NeRF employs a hierarchical sampling scheme. Two networks are trained simultaneously: coarse (or proposal) and fine. Firstly, the coarse network is evaluated on a uniform grid of N_c points and a set of weights w_i is calculated as in Eq. 5. Normalizing these weights produces a piecewise-constant PDF along the ray. Then N_f samples are drawn from this distribution and the union of the first and the second sets of points is used to evaluate the fine network and compute the final color estimation. The coarse network is also trained to predict ground truth colors, but the color estimate for the coarse network is calculated only using the first set of N_c points.

3. Reparameterized Volume Sampling and Radiance Estimates

3.1. Reparameterized Expected Radiance Estimates

Monte Carlo method gives a natural way to approximate the expected color. For example, given k i.i.d. samples $t_1, \dots, t_k \sim p_r(t)$ and the normalization constant $y_f := \int_{t_n}^{t_f} p_r(t) dt$, the sum

$$\hat{C}_{MC}(r) = \frac{y_f}{k} \sum_{i=1}^k c_r(t_i) \quad (6)$$

is an unbiased estimate of the expected radiance in Eq. 2. Moreover, samples t_1, \dots, t_k belong to high-density regions of p_r by design, thus for a degenerate density p_r even a few samples would provide an estimate with low variance. Importantly, unlike the approximation in Eq. 4, the Monte Carlo estimate depends on scene density σ implicitly through sampling algorithm and requires a custom gradient estimate for the parameters of σ . We propose a principled end-to-end differentiable algorithm to generate samples from $p_r(t)$.

Our solution is primarily inspired by the reparameterization trick (Kingma & Ba, 2014; Rezende et al., 2014). We change the variable in Eq. 2. For $F_r(t) := 1 - \exp\left(-\int_{t_n}^t \sigma_r(s) ds\right)$ and $y := F_r(t)$ we rewrite

$$C(r) = \int_{t_n}^{t_f} c_r(t) p_r(t) dt \quad (7)$$

$$= \int_{y_n}^{y_f} c_r(F_r^{-1}(y)) dy \quad (8)$$

$$= \int_0^1 y_f c_r(F_r^{-1}(y_f u)) du. \quad (9)$$

The integral boundaries are $y_n := F_r(t_n) = 0$ and $y_f := F_r(t_f)$. Function $F_r(t)$ acts as the cumulative distribution function of the variable t with a single exception that, in general, $F_r(t_f) \neq 1$. In volume rendering, $F_r(t)$ is called opacity function with y_f being equal to overall pixel opaqueness. After the first change of variables in Eq. 8, the integral boundaries depend on opacity F_r and, as consequence, on ray density σ_r . We further simplify the integral by changing the integration boundaries to $[0, 1]$ and substituting $y_n = 0$.

Given the above derivation, we construct the *reparameterized Monte Carlo estimate* for the right-hand side integral in Eq. 9

$$\hat{C}_{MC}^R(r) := \frac{y_f}{k} \sum_{i=1}^k c_r(F_r^{-1}(y_f u_i)), \quad (10)$$

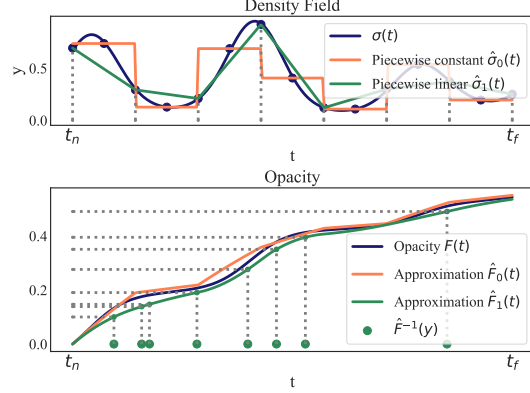


Figure 2: Illustration of opacity inversion. On the left, we approximate density field σ_r with a piecewise constant and a piecewise linear approximation. On the right, we approximate opacity $F_r(t)$ and compute $F_r^{-1}(y_f u)$ for $u \sim U[0, 1]$.

with k i.i.d. $U[0, 1]$ samples u_1, \dots, u_k . It is easy to show that estimate in Eq. 10 is an unbiased estimate of expected color in Eq. 2 and its gradient is an unbiased estimate of the gradient of the expected color $C(r)$. Additionally, we propose to replace the uniform samples u_1, \dots, u_k with uniform independent samples within regular grid bins $v_i \sim U\left[\frac{i-1}{k+1}, \frac{i}{k+1}\right], i = 1, \dots, k$. The latter samples yield a stratified variant of the estimate in Eq. 10 and, most of the time, leads to lower variance estimates (see Appendix 5.2).

In the above estimate, random samples u_1, \dots, u_k do not depend on volume density σ_r or color c_r . Essentially, for the reparameterized Monte Carlo estimate we generate samples from $p_r(t)$ using inverse cumulative distribution function $F_r^{-1}(y_f u)$. In what follows, we coin the term *reparameterized volume sampling (RVS)* for the sampling procedure. However, in practice we cannot compute F_r analytically and can only query σ_r at certain ray points. Thus, in the following section, we introduce approximations of F_r and its inverse.

3.2. Opacity Approximations

Expected radiance estimate in Eq. 10 relies on opacity $F_r(t) = 1 - \exp\left(-\int_{t_n}^t \sigma_r(s) ds\right)$ and its inverse $F_r^{-1}(y)$. We propose to approximate the opacity using a piecewise density field approximation. Fig. 2 illustrates the approximations and ray samples obtained through opacity inversion. To construct the approximation, we take a grid $t_n = t_0 < t_1 < \dots < t_m = t_f$ and construct either a piecewise constant or a piecewise linear approximations. In the former case, we pick a point within each bin $t_i \leq \hat{t}_i \leq t_{i+1}$ and approximate density with $\sigma_r(\hat{t}_i)$ inside the corresponding bin. In the latter case, we compute σ_r in the grid points

and interpolate the values between the grid points. Importantly, for a non-negative field these two approximations are also non-negative. Then we compute $\int_{t_n}^t \sigma_r(s)ds$, which is a sum of rectangular areas in the piecewise constant case

$$I_0(t) = \sum_{j=1}^i \sigma_r(\hat{t}_j)(t_j - t_{j-1}) + \sigma_r(\hat{t}_i)(t - t_i). \quad (11)$$

Analogously, the integral approximation $I_1(t)$ in the piecewise linear case is a sum of trapezoidal areas.

Given these approximations, we can approximate y_f and F_r in Eq. 10. We generate samples on a ray based on inverse opacity $F_r^{-1}(y)$ by solving the equation

$$y_f u = F_r(t) = 1 - \exp\left(-\int_{t_n}^t \sigma_r(s)ds\right) \quad (12)$$

for t , where $u \in [0, 1]$ is a random sample. We rewrite the equation as $-\log(1 - y_f u) = \int_{t_n}^t \sigma_r(s)ds$ and note that integral approximations $I_0(t)$ and $I_1(t)$ are monotonic piecewise linear and piecewise quadratic functions. We obtain the inverse by first finding the bin that contains the solution and then solving a linear or a quadratic equation. Crucially, the solution t can be seen as a differentiable function of density field σ_r and we can back-propagate the gradients w.r.t. σ_r through t . We provide explicit formulae for t for both approximations in Appendix A.1 and discuss the solutions crucial for the numerical stability in Appendix A.2. We use piecewise linear approximation in Section 5.1 and piecewise constant approximations in Section 5.3.

3.3. Application to Hierarchical Sampling

Finally, we propose to apply our RVS algorithm to the hierarchical sampling scheme originally proposed in NeRF. The method we introduce consists of two changes to the original scheme. Firstly, we replace sampling from piecewise-constant PDF along the ray defined by weights w_i (see Section 2) with our sampling algorithm that uses piecewise linear approximation of σ_r and generates samples from $p_r(t)$ using inverse CDF. Secondly, we remove the auxiliary reconstruction loss imposed on the coarse network. Instead, we propagate gradients through sampling. This way, we eliminate the need for auxiliary coarse network losses and train the network to solve the actual task of our interest: picking the best points for evaluation of the fine network. In Subsection 5.1, we refer to the coarse network as the proposal network, since such naming better captures its purpose.

4. Related Work

Monte-Carlo estimates for integral approximations. In this work, we revisit the algorithm introduced to approx-

imate the expected color in (Max, 1995). Currently, it is the default solution in multiple of works on neural radiance fields. (Max, 1995) approximate density and radiance fields with a piecewise constant functions along a ray and compute Eq. 2 as an approximation. Instead, we reparameterize Eq. 2 and construct Monte-Carlo estimates for the integral. To compute the estimates in practice we use piecewise approximations only for the density field. The cumulative density function (CDF) used in our estimates involves integrating density field along a ray. (Lindell et al., 2021) construct field anti-derivatives to accelerate inference. While they use the anti-derivatives to compute 2 on a grid with fewer knots, the anti-derivatives can be applied in our sampling method based on the inverse CDF without resorting to piecewise approximations.

In the past decade, integral reparameterizations became a common practice in generative modeling (Kingma & Welling, 2013; Rezende et al., 2014) and approximate Bayesian inference (Blundell et al., 2015; Gal & Ghahramani, 2016; Molchanov et al., 2017). Similar to Equation 2, objectives in these areas require optimizing expected values with respect to distribution parameters. We refer readers to (Mohamed et al., 2020) for a systematic overview. Notably, in computer graphics, (Loube et al., 2019) apply reparameterization to estimate gradients of path traced images with respect to scene parameters.

NeRF acceleration through architecture and sparsity. Since the original NeRF work (Mildenhall et al., 2020), a number of approaches that aim to improve the efficiency of the model have been proposed. One family of methods tries to reduce the time required to evaluate the field. It includes a variety of architectures combining Fourier features (Tancik et al., 2020) and grid-based features (Garbin et al., 2021; Sun et al., 2021; Yu et al., 2021a; Reiser et al., 2021). Besides grids, some works exploit space partitions based on Voronoi diagrams (Rebain et al., 2021), trees (Hu et al., 2022; Yu et al., 2021b) and even hash tables (Müller et al., 2022). These architectures generally trade-off inference speed for parameter count. TensorRF (Chen et al., 2022) stores the grid tensors in a compressed format to achieve both high compression and fast performance. On top of that, skipping field queries for the empty parts of a scene additionally improves rendering time (Levoy, 1990). Recent works (such as (Hedman et al., 2021; Fridovich-Keil et al., 2022; Liu et al., 2020; Li et al., 2022; Sun et al., 2021; Müller et al., 2022)) manually exclude low-weight components in Eq 4 to speed up rendering during training and inference. Below we show that our algorithm is compatible with sparse density fields and achieves comparable speed up by using a few radiance evaluations.

Anti-aliased scene representations. Mip-NeRF (Barron et al., 2021) and Mip-NeRF 360 (Barron et al., 2022) repre-

sent a line of work that modifies scene representations. Mip-NeRF propose to use conical frustums instead of ray points, which in turn allows the model to represent the scene at a continuously-valued scale. Mip-NeRF 360 further extends Mip-NeRF by introducing a contraction operator that allows to represent unbounded scenes. More relevant to our research is the fact that these models employ modifications of the original hierarchical sampling scheme where the coarse network parameterizes some density field. Mip-NeRF parameterizes the coarse and the fine fields by the same neural network that represents the scene at a continuously-valued scale. Mip-NeRF 360 uses a separate network for coarse density, but trains it to mimick the fine density rather than reconstructing the image. This means that our method for training the proposal density field can be potentially used to improve the performance of these models.

Algorithms for picking ray points. (Mildenhall et al., 2020) employs a hierarchical scheme to generate ray points using an auxiliary density and color fields. Since then, a number of other methods for picking ray points, which focus on real-time rendering and aim to improve the efficiency of NeRF, have been proposed. DoNeRF (Neff et al., 2021) uses a designated depth oracle network supervised with ground truth depth maps. TermiNeRF (Piala & Clark, 2021) foregoes the depth supervision by distilling the sampling network from a pre-trained NeRF model. NeRF-ID (Arandjelović & Zisserman, 2021) adds a separate differentiable proposer network to the original NeRF model that maps outputs of the coarse network into a new set of samples. The model is trained in two stage procedure together with NeRF. Authors of NeuSample (Fang et al., 2021) use a sample field that directly transforms rays into point coordinates. Sample field can be further fine-tuned for rendering with smaller number of samples. AdaNeRF (Kurz et al., 2022) proposes to use a sampling and a shading network. Samples from sampling network are processed by shading network that tries to predict the importance of samples and cull the samples with low importance. These works focus on speeding up rendering and do not directly aim at speeding up training or improving the rendering quality. On the contrary, our approach to differentiable hierarchical sampling modifies the way the proposal (coarse in the original NeRF work) density field is trained and in turn aims at refining the training procedure and improving the reconstruction quality of the obtained NeRF model.

5. Experiments

5.1. End-to-end Differentiable Hierarchical Sampling

In this section, we evaluate the proposed approach to hierarchical volume sampling on the original NeRF model.

Experimental setup. We do the comparison by fixing some training setup and training two models from scratch: one model is trained using the procedure proposed in (Mildenhall et al., 2020) (further denoted as NeRF in the results), and the other one is trained using our modification described in Subsection 3.3 (further denoted as RVS). For both models, the final color approximation is computed as in Eq. 4, so the difference only appears in the proposal component.

We trained all models for 500k iterations using the same hyperparameters as in the original paper with minor differences. We replaced ReLU density output activation with Softplus. The other difference is that we used smaller learning rate for the proposal network in our method (start with 5×10^{-5} and decay to 5×10^{-6}) but the same for the fine network (start with 5×10^{-4} and decay to 5×10^{-5}). We observed that decreasing the proposal network learning rate improves stability of our method. We ran the default NeRF training algorithm in our experiments with the same learning rates for proposal and fine networks. Further in the ablation study we show that decreasing proposal network learning rate only decreases the performance of the base algorithm. We used PyTorch implementation (Yen-Chen, 2020) of NeRF in our experiments.

Table 1: Comparison on the Lego scene of Blender dataset between NeRF training algorithm and our modification depending on the number of proposal and fine network evaluations per ray (N_p, N_f). The (64, 192) configuration is the one originally used in NeRF. Training time column depicts relative training time on NVIDIA A100 GPU.

	Evaluations N_p	N_f	Train time	PSNR \uparrow	SSIM \uparrow	LPIPS \downarrow
NeRF	16	32	0.39	27.09	0.913	0.121
RVS	16	32	0.37	29.18	0.928	0.112
NeRF	32	64	0.52	30.11	0.947	0.070
RVS	32	64	0.48	31.89	0.955	0.066
NeRF	64	128	0.79	32.14	0.958	0.053
RVS	64	128	0.76	32.80	0.963	0.051
NeRF	64	192	1.0	32.69	0.962	0.048
RVS	64	192	0.98	33.03	0.964	0.047

Comparative evaluation. We start the comparison on the Lego scene of the Blender dataset (Mildenhall et al., 2020) for different (N_p, N_f) configurations that correspond to number of proposal and fine network evaluations. Note that this N_p, N_f notation does not directly correspond to the N_c, N_f notation used in Section 2 since the original NeRF model evaluates the fine network in $N_c + N_f$ points. For more details on training configurations and options for picking points for fine network evaluation, see Appendix C. The results are presented in Table 1. Our method outperformed the baseline across all configurations and all metrics, with the only exception of LPIPS in (64, 192) configuration, where it showed similar performance. We observe that the

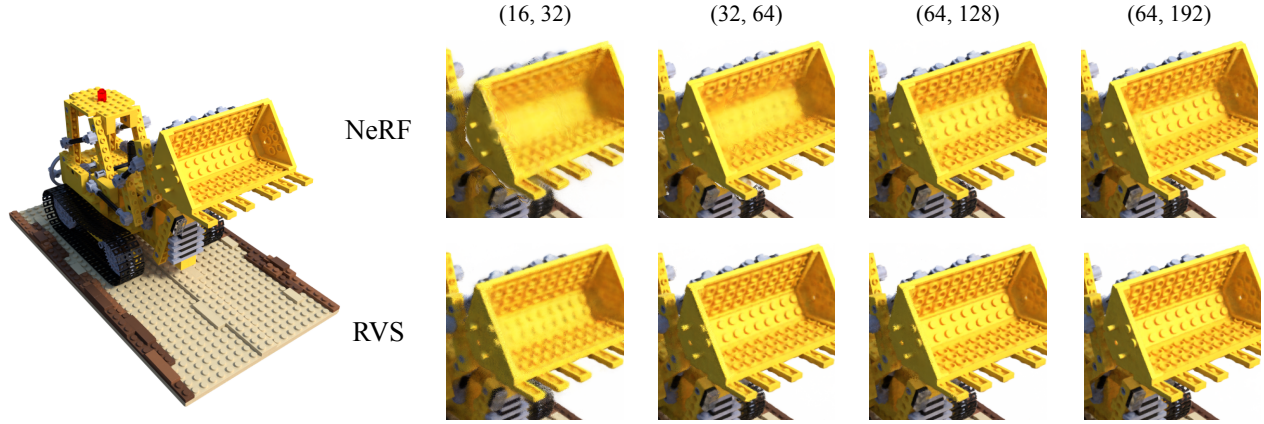


Figure 3: Comparison between renderings of test-set view on the Lego scene (Blender). Rows correspond to different (N_p, N_f) configurations. NeRF baseline has difficulties in reconstructing fine details for $(16, 32)$ and $(32, 64)$ configurations, and some parts remain blurry even in $(64, 128)$ and $(64, 192)$ configurations, while our method already produces realistic reconstruction for $(32, 64)$ configuration.

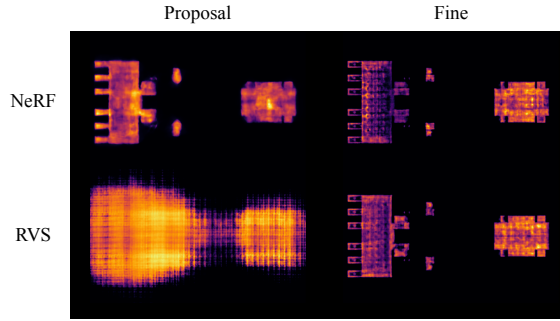


Figure 4: Visualizations across 2D slice of proposal and fine densities learnt on the Lego scene in $(32, 64)$ configuration. Brighter pixels correspond to larger density values.

improvement is more significant for smaller (N_p, N_f) . Our method also has a minor speedup over the baseline due to the fact that the former does not use the radiance component of the proposal network. Fig. 3 in visualizes test-set view renderings of models trained by two methods.

We also visualize proposal and fine densities learned by two algorithms in Fig. 4. Figures are constructed by fixing some value of z coordinate and calculating the density on (x, y) -plane. While fine density visualizations look very similar, proposal densities turn out very different. This happens due to the fact that the original algorithm trains the proposal network to reconstruct the scene (but using smaller number of points for color estimation), while our algorithm trains this network to sample points for fine network evaluation that would lead to a better overall reconstruction. We believe that this may also explain the improved rendering quality that our method shows.

Next, we evaluated our method on all scenes from Blender and LLFF (Mildenhall et al., 2019) datasets. Table 2 depicts the results averaged across all scenes. The results for individual scenes can be found in Table 9 and Table 10 in Appendix. Our approach showed improvement over the baseline on all scenes of Blender dataset. While the improvement is less pronounced on LLFF dataset, it is still present across all metrics on average. Fig. 9 in Appendix visually depicts the quality of reconstruction on T-Rex scene.

Table 2: Comparison on Blender and LLFF datasets in $(N_p = 32, N_f = 64)$ configuration.

	Blender Dataset		
	PSNR \uparrow	SSIM \uparrow	LPIPS \downarrow
NeRF	29.49	0.934	0.085
RVS	30.26	0.939	0.082
LLFF Dataset			
	PSNR \uparrow	SSIM \uparrow	LPIPS \downarrow
	26.01	0.796	0.273
NeRF	26.24	0.799	0.270
RVS			

Ablation study. Finally, we ablated the influence of some components of our approach on the results. Table 3 presents the ablation study results. Firstly, we ran the baseline with decreased learning rate for the proposal network, thus fully matching all training hyperparameters with our method. This only reduced all metrics in comparison to the baseline. Then, we ran our approach, but replaced our algorithm that draws samples from the proposal distribution with the sampling algorithm originally proposed in NeRF. Even though the original work does not propagate gradients through sampling, the algorithm is still end-to-end differentiable, thus

Table 3: Ablation study on Blender dataset in ($N_p = 32, N_f = 64$) configuration.

	Blender Dataset		
	PSNR \uparrow	SSIM \uparrow	LPIPS \downarrow
NeRF (decreased prop. lr)	29.23	0.932	0.090
NeRF (union of points)	29.06	0.929	0.096
NeRF	29.49	0.934	0.085
RVS (base sampling)	29.07	0.929	0.095
RVS	30.26	0.939	0.082

the setup is plausible. It also produced results that fell behind the baseline. Finally, we ran the baseline with different strategy for picking fine points (see Appendix C for detailed discussion), which also led to degradation of the baseline performance.

5.2. Radiance Estimates for a Single Ray

In this section, we evaluate the proposed Monte Carlo radiance estimate (see Eq. 10) in a one-dimensional setting. In this experiment, we assume that we know density in advance and show how the estimate variance depends on number of radiance calls. Compared to sampling approaches, the standard approximation from Eq. 4 has zero variance but does not allow controlling number of radiance calls.

Our experiment models light propagation on a single ray in two typical situations. The upper row of Fig. 5 defines a scalar radiance field (orange) $c_r(t)$ and opacity functions (blue) $F_r(t)$ for "Foggy" and "Wall" density fields. The first models a semi-transparent volume, which often occurs after model initialization during training. In the second light is emitted from a single point on a ray, which is common in applications.

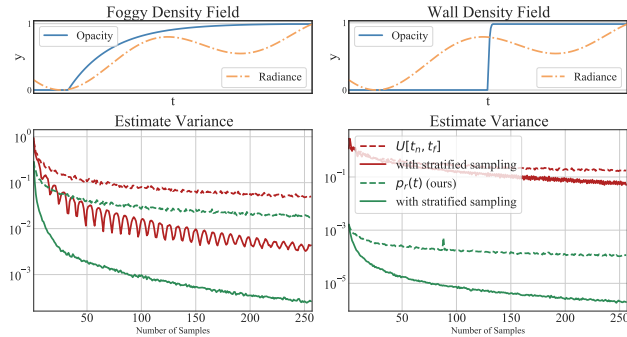


Figure 5: Color estimate variance compared for a varying number of samples. The upper plot illustrates underlying opacity function on a ray; the lower graph depicts variance in logarithmic scale. Compared to a naive estimate of the integral with uniform samples (dashed red), inverse transform sampling exhibits lower variance (dashed green). Stratified sampling improves variance in both setups (solid lines).

For the two fields we estimated the expected radiance $C(\mathbf{r}) = \int_{t_n}^{t_f} c_r(t) dF_r(t)$. We considered two baseline methods (both in red in Fig. 5): the first was a Monte Carlo estimate of C obtained with uniform distribution on a ray $U[t_n, t_f]$, and its stratified modification with a uniform grid $t_n = t_0 < \dots < t_k = t_f$ (note that here we use k to denote the number of samples, not the number of grid points m in piecewise density approximation):

$$\hat{C}_{\text{IW}}(\mathbf{r}) = \sum_{i=1}^k (t_i - t_{i-1}) c_r(\tau_i) \frac{dF_r}{dt} \Big|_{t=\tau_i}, \quad (13)$$

where $\tau_i \sim U[t_{i-1}, t_i]$ are independent uniform bin samples. We compared the baseline against estimate from Eq. 10 and its stratified modification. All estimates are unbiased. Therefore, we only compared the estimates variances for a varying number of samples m . In all setups, our stratified estimate uniformly outperformed the baselines. For the more challenging "foggy" field, approximately $k = 32$ samples were required to match the baseline performance for $k = 128$. We matched the baseline with only a $k = 4$ samples for the "wall" field. Inverse transform sampling requires only a few points for degenerate distributions.

5.3. Scene Reconstruction with Monte Carlo Estimates

In this section, we evaluate the proposed Monte Carlo radiance estimate as a part of rendering algorithm for scene reconstruction. Given an accurate density field approximation, our color estimate is unbiased for any given number of samples k . Therefore, our estimate is especially suitable for architectures that can evaluate the density field faster than the radiance field. As an example, we picked a recent voxel-based radiance field model DVGO (Sun et al., 2021) that parametrizes density field as a voxel grid and relies on a combination of voxel grid and a view-dependent neural network to parameterize radiance. In our experiments, we took the default model parameters and only replaced the rendering algorithm.

Table 4: Training iteration times and peak memory consumption for different color approximations.

DVGO Renderer	Speed	Memory
Default w/o sparsity	24 it/s	9 GB
Default w/ sparsity	160 it/s	5 GB
MC + RVS, $k = 128$	20 it/s	8 GB
MC + RVS, $k = 8$	170 it/s	5 GB
MC + RVS, $k = 1$	260 it/s	5 GB

Experimental setup & comparative evaluation. In Table 4, we report iterations per second and peak memory consumption on the Lego scene of Blender dataset during training. One of the primary goals of DVGO was to reduce

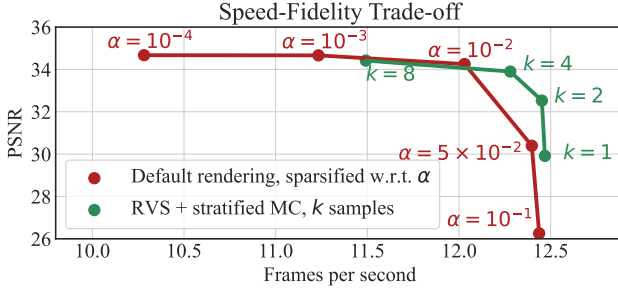


Figure 6: Test-time rendering quality as a function of rendering speed. Given a scene representation pre-trained with the standard rendering algorithm, we evaluate rendering algorithms at various configurations.

Table 5: Scene reconstruction results for Blender dataset.

DVGO Renderer	Time (min)	PSNR \uparrow	SSIM \uparrow	LPIPS \downarrow
Default w/ sparsity	2:48	31.90	0.956	0.054
MC + RVS, $k = 4$	2:24	31.19	0.951	0.059
MC + RVS, $k = 8$	2:00	31.13	0.951	0.059
MC + RVS, adaptive k	2:54	31.44	0.953	0.056

the training time of a scene model. To achieve that goal, the authors mask components in the sum in Eq. 4 that have weights below a certain threshold α . We achieve a similar effect without thresholding: $k = 8$ samples yield a comparable $\times 6$ speed up and with fewer samples, we reduce iteration time even further. However, the speed-up in our estimate comes at cost of additional estimate variance. Next, we evaluated the effect of additional variance on the rendering fidelity. In Fig. 6, we report test PSNR on a fixed pre-trained Lego scene representation for both rendering algorithms. Our algorithm achieves the same average PSNR with k samples and even outperforms the default rendering algorithm with a higher sparsity threshold α .

In Table 5, we report the performance of models trained with various color estimates (see Appendix E for per-scene results). We trained a model with $k = 4$ samples using $\times \frac{3}{2}$ more training steps than with $k = 8$ samples aiming to achieve similar training times. Additionally, we considered a model that chooses the number of samples k on each ray adaptively between 4 and 48 based on the number of grid points with high density. The adaptive number of samples allowed to reduce estimate variance without a drastic increase in training time. We evaluate our models with $k = 64$ samples to mitigate the effect of variance on evaluation. As Table 5 indicates, the training algorithm with our color approximation yields worse scene reconstruction quality compared to the default.

Ablation study. We ablated the proposed algorithm on the Lego scene to gain further insights into the difference in

Table 6: Ablation study of the Lego scene.

Ablated Feature	PSNR
MC + RVS with adaptive k	33.85
Training steps ($\times 7$)	+0.28
Training steps ($\times 7$)	+0.28
Monte Carlo samples ($\times 2$ on avg.)	+0.15
Dense grid on rays ($\times 2$)	+0.29
Unbiased loss $L_2(\mathbb{E}\hat{C}, C_{gt})$	+0.25
Density grid resolution ($160^3 \rightarrow 256^3$)	+0.63
Radiance grid resolution ($160^3 \rightarrow 256^3$)	+0.08
$\sigma + c$ resolution ($160^3 \rightarrow 256^3$)	+0.86
DVGO	34.64

reconstruction fidelity. Specifically, we ablated parameters affecting optimization aiming to match the reconstruction quality of the default algorithm. The results are given in Table 6. The increase in training steps or the number of samples improved the performance but did not lead to matching results. Increased spline density improved both our model and the baseline to the same extent. We also noticed that the standard objective estimated the expected loss $\mathbb{E}L_2(\hat{C}, C_{gt})$ rather than the loss at expected radiance $L_2(\mathbb{E}\hat{C}, C_{gt})$ which leads to an additional bias towards low-variance densities. The estimate $(\hat{C}_1 - C_{gt})(\hat{C}_2 - C_{gt})$ with two i.i.d. color estimates is an unbiased estimate of the latter and allows reconstructing non-degenerate density fields, but the estimate has little effect in case of degenerate densities omnipresent in 3D scenes. Finally, with denser ray grid our algorithm surpassed the baseline PSNR of 34.67 at twice the training time. For qualitative comparison, in Appendix D, we visualize the differences in reconstructed models and in renders reported in Fig. 6.

To summarise, training with reparameterized volume sampling currently does not match the fidelity of the standard approach. At the same time, Monte Carlo radiance estimates provide a straightforward mechanism to control both training and inference speed. Our ablation study shows that lower reconstruction fidelity cannot be fully attributed to the estimate variance and needs better understanding of training dynamics.

6. Conclusion

We proposed an alternative rendering algorithm for novel view synthesis models based on radiance fields. The core of our contribution is an end-to-end differentiable ray point sampling algorithm. Our rendering algorithm provides an explicit mechanism to control rendering time during the inference and training stages. Compared to the standard rendering algorithm, we achieve inferior reconstruction quality, that suggests areas for future research. At the same time, we show that the underlying sampling algorithm improves

scene reconstruction in hierarchical models and simplifies the training approach by disposing of auxiliary losses.

Acknowledgements

The study was carried out within the strategic project "Digital Transformation: Technologies, Effects and Performance", part of the HSE University "Priority 2030" Development Programme. This research was supported in part through computational resources of HPC facilities at HSE University.

References

- Arandjelović, R. and Zisserman, A. Nerf in detail: Learning to sample for view synthesis. *arXiv preprint arXiv:2106.05264*, 2021.
- Barron, J. T., Mildenhall, B., Tancik, M., Hedman, P., Martin-Brualla, R., and Srinivasan, P. P. Mip-nerf: A multiscale representation for anti-aliasing neural radiance fields. In *Proceedings of the IEEE/CVF International Conference on Computer Vision*, pp. 5855–5864, 2021.
- Barron, J. T., Mildenhall, B., Verbin, D., Srinivasan, P. P., and Hedman, P. Mip-nerf 360: Unbounded anti-aliased neural radiance fields. In *Proceedings of the IEEE/CVF Conference on Computer Vision and Pattern Recognition*, pp. 5470–5479, 2022.
- Blundell, C., Cornebise, J., Kavukcuoglu, K., and Wierstra, D. Weight uncertainty in neural network. In *International conference on machine learning*, pp. 1613–1622. PMLR, 2015.
- Chen, A., Xu, Z., Geiger, A., Yu, J., and Su, H. Tensorf: Tensorial radiance fields. *arXiv preprint arXiv:2203.09517*, 2022.
- Fang, J., Xie, L., Wang, X., Zhang, X., Liu, W., and Tian, Q. Neusample: Neural sample field for efficient view synthesis. *arXiv preprint arXiv:2111.15552*, 2021.
- Figurnov, M., Mohamed, S., and Mnih, A. Implicit reparameterization gradients. *Advances in Neural Information Processing Systems*, 31, 2018.
- Fridovich-Keil, S., Yu, A., Tancik, M., Chen, Q., Recht, B., and Kanazawa, A. Plenoxels: Radiance fields without neural networks. In *Proceedings of the IEEE/CVF Conference on Computer Vision and Pattern Recognition*, pp. 5501–5510, 2022.
- Gal, Y. and Ghahramani, Z. Dropout as a bayesian approximation: Representing model uncertainty in deep learning. In *international conference on machine learning*, pp. 1050–1059. PMLR, 2016.
- Garbin, S. J., Kowalski, M., Johnson, M., Shotton, J., and Valentin, J. Fastnerf: High-fidelity neural rendering at 200fps. In *Proceedings of the IEEE/CVF International Conference on Computer Vision*, pp. 14346–14355, 2021.
- Hedman, P., Srinivasan, P. P., Mildenhall, B., Barron, J. T., and Debevec, P. Baking neural radiance fields for real-time view synthesis. In *Proceedings of the IEEE/CVF International Conference on Computer Vision*, pp. 5875–5884, 2021.
- Hu, T., Liu, S., Chen, Y., Shen, T., and Jia, J. Efficientnerf efficient neural radiance fields. In *Proceedings of the IEEE/CVF Conference on Computer Vision and Pattern Recognition*, pp. 12902–12911, 2022.
- Kingma, D. P. and Ba, J. Adam: A method for stochastic optimization. *arXiv preprint arXiv:1412.6980*, 2014.
- Kingma, D. P. and Welling, M. Auto-encoding variational bayes. *arXiv preprint arXiv:1312.6114*, 2013.
- Kurz, A., Neff, T., Lv, Z., Zollhöfer, M., and Steinberger, M. Adanerf: Adaptive sampling for real-time rendering of neural radiance fields. In *Computer Vision–ECCV 2022: 17th European Conference, Tel Aviv, Israel, October 23–27, 2022, Proceedings, Part XVII*, pp. 254–270. Springer, 2022.
- Levoy, M. Efficient ray tracing of volume data. *ACM Transactions on Graphics (TOG)*, 9(3):245–261, 1990.
- Li, R., Tancik, M., and Kanazawa, A. Nerfacc: A general nerf acceleration toolbox. *arXiv preprint arXiv:2210.04847*, 2022.
- Lindell, D. B., Martel, J. N., and Wetzstein, G. Autoint: Automatic integration for fast neural volume rendering. In *Proceedings of the IEEE/CVF Conference on Computer Vision and Pattern Recognition*, pp. 14556–14565, 2021.
- Liu, L., Gu, J., Zaw Lin, K., Chua, T.-S., and Theobalt, C. Neural sparse voxel fields. *Advances in Neural Information Processing Systems*, 33:15651–15663, 2020.
- Loubet, G., Holzschuch, N., and Jakob, W. Reparameterizing discontinuous integrands for differentiable rendering. *ACM Transactions on Graphics (TOG)*, 38(6):1–14, 2019.
- Max, N. Optical models for direct volume rendering. *IEEE Transactions on Visualization and Computer Graphics*, 1(2):99–108, 1995.
- Mildenhall, B., Srinivasan, P. P., Ortiz-Cayon, R., Kalantari, N. K., Ramamoorthi, R., Ng, R., and Kar, A. Local light field fusion: Practical view synthesis with prescriptive sampling guidelines. *ACM Transactions on Graphics (TOG)*, 38(4):1–14, 2019.

- Mildenhall, B., Srinivasan, P. P., Tancik, M., Barron, J. T., Ramamoorthi, R., and Ng, R. Nerf: Representing scenes as neural radiance fields for view synthesis. In *European conference on computer vision*, pp. 405–421. Springer, 2020.
- Mohamed, S., Rosca, M., Figurnov, M., and Mnih, A. Monte carlo gradient estimation in machine learning. *J. Mach. Learn. Res.*, 21(132):1–62, 2020.
- Molchanov, D., Ashukha, A., and Vetrov, D. Variational dropout sparsifies deep neural networks. In *International Conference on Machine Learning*, pp. 2498–2507. PMLR, 2017.
- Müller, T., Evans, A., Schied, C., and Keller, A. Instant neural graphics primitives with a multiresolution hash encoding. *arXiv preprint arXiv:2201.05989*, 2022.
- Neff, T., Stadlbauer, P., Parger, M., Kurz, A., Mueller, J. H., Chaitanya, C. R. A., Kaplanyan, A., and Steinberger, M. Donerf: Towards real-time rendering of compact neural radiance fields using depth oracle networks. In *Computer Graphics Forum*, volume 40, pp. 45–59. Wiley Online Library, 2021.
- Piala, M. and Clark, R. Terminerf: Ray termination prediction for efficient neural rendering. In *2021 International Conference on 3D Vision (3DV)*, pp. 1106–1114. IEEE, 2021.
- Rebain, D., Jiang, W., Yazdani, S., Li, K., Yi, K. M., and Tagliasacchi, A. Derf: Decomposed radiance fields. In *Proceedings of the IEEE/CVF Conference on Computer Vision and Pattern Recognition*, pp. 14153–14161, 2021.
- Reiser, C., Peng, S., Liao, Y., and Geiger, A. Kilonerf: Speeding up neural radiance fields with thousands of tiny mlps. In *Proceedings of the IEEE/CVF International Conference on Computer Vision*, pp. 14335–14345, 2021.
- Rezende, D. J., Mohamed, S., and Wierstra, D. Stochastic backpropagation and approximate inference in deep generative models. In *International conference on machine learning*, pp. 1278–1286. PMLR, 2014.
- Sun, C., Sun, M., and Chen, H.-T. Direct voxel grid optimization: Super-fast convergence for radiance fields reconstruction. *arXiv preprint arXiv:2111.11215*, 2021.
- Tancik, M., Srinivasan, P., Mildenhall, B., Fridovich-Keil, S., Raghavan, N., Singhal, U., Ramamoorthi, R., Barron, J., and Ng, R. Fourier features let networks learn high frequency functions in low dimensional domains. *Advances in Neural Information Processing Systems*, 33: 7537–7547, 2020.
- Yen-Chen, L. Nerf-pytorch. <https://github.com/yenchenlin/nerf-pytorch/>, 2020.
- Yu, A., Fridovich-Keil, S., Tancik, M., Chen, Q., Recht, B., and Kanazawa, A. Plenoxels: Radiance fields without neural networks. *arXiv preprint arXiv:2112.05131*, 2021a.
- Yu, A., Li, R., Tancik, M., Li, H., Ng, R., and Kanazawa, A. Plenoctrees for real-time rendering of neural radiance fields. In *Proceedings of the IEEE/CVF International Conference on Computer Vision*, pp. 5752–5761, 2021b.

A. Inverse Opacity Calculation

A.1. Inverse Functions for Density Integrals

In this section, we derive explicit formulae for the density integral inverse used in inverse opacity.

A.1.1. PIECEWISE CONSTANT APPROXIMATION INVERSE

We start with a formula for the integral

$$I_0(t) = \sum_{j=1}^i \sigma_r(\hat{t}_j)(t_j - t_{j-1}) + \sigma_r(\hat{t}_i)(t - t_i) \quad (14)$$

and solve for t equation

$$y = I_0(t). \quad (15)$$

The equation above is a linear equation with solution

$$t = t_i + \frac{y - \sum_{j=1}^i \sigma_r(\hat{t}_j)(t_j - t_{j-1})}{\sigma_r(\hat{t}_i)}. \quad (16)$$

In our implementation we add small ϵ to the denominator to improve stability when $\sigma_r(\hat{t}_i) \approx 0$.

A.1.2. PIECEWISE LINEAR APPROXIMATION INVERSE

The piecewise linear density approximation yield a piecewise quadratic function

$$I_1(t) = \sum_{j=1}^i \frac{\sigma_r(t_j) + \sigma_r(t_{j-1})}{2}(t_j - t_{j-1}) + \frac{(\sigma_r(t_i) + \bar{\sigma}_r(t))}{2}(t - t_i), \quad (17)$$

where $\bar{\sigma}_r(t) = \sigma_r(t_i) \frac{t_{i+1}-t}{t_{i+1}-t_i} + \sigma_r(t_{i+1}) \frac{t-t_i}{t_{i+1}-t_i}$ is the interpolated density at t . Again, we solve

$$y = I_1(t) \quad (18)$$

for t . We change the variable to $\Delta t := t - t_i$ and note that terms a and c in quadratic equation

$$0 = a\Delta t^2 + b\Delta t + c \quad (19)$$

will be

$$a = \frac{\sigma_r(t_{i+1}) - \sigma_r(t_i)}{2} \quad (20)$$

$$c = \left(\sum_{j=1}^i \frac{\sigma_r(t_j) + \sigma_r(t_{j-1})}{2}(t_j - t_{j-1}) - y \right) \times (t_{i+1} - t_i) \quad (21)$$

and with a few algebraic manipulations we find the linear term

$$b = \sigma_r(t_i) \times (t_{i+1} - t_i). \quad (22)$$

Since our integral monotonically increases, we can deduce that the root Δt must be

$$\Delta t = \frac{-b + \sqrt{b^2 - 4ac}}{2a}. \quad (23)$$

However, this root is computationally unstable when $a \approx 0$. The standard trick is to rewrite the root as

$$\Delta t = \frac{2c}{b + \sqrt{b^2 - 4ac}}. \quad (24)$$

For computational stability, we add small ϵ to the square root argument. See the supplementary notebook for details.

A.2. Numerical Stability in Inverse Opacity

Inverse opacity input y is a combination of a uniform sample u and ray opacity $y_f = 1 - \exp\left(-\int_{t_n}^{t_f} \sigma_r(s)ds\right)$:

$$y = -\log(1 - y_f u). \quad (25)$$

The expression above is a combination of a logarithm and exponent. We rewrite it to replace with more reliable logsumexp operator:

$$y = -\log\left(\exp(\log(1-u)) + \exp(\log u - \int_{t_n}^{t_f} \sigma_r(s)ds)\right). \quad (26)$$

In practice, for opaque rays $\int_{t_n}^{t_f} \sigma_r(s)ds \approx 0$ implementation of logsumexp becomes computationally unstable. In this case, we replace y with a first order approximation $u \cdot \int_{t_n}^{t_f} \sigma_r(s)ds$.

A.3. Implicit Inverse Opacity Gradients

To compute the estimates in Eq. 10, we need to compute the inverse opacity $F_r^{-1}(y)$ along with its gradient. In the main paper, we invert opacity explicitly with a differentiable algorithm. Alternatively, we could invert $F_r(t) = 1 - \exp\left(-\int_{t_n}^t \sigma_r(s)ds\right)$ with binary search.

Opacity $F_r(t)$ is a monotonic function and for $y \in (y_n, y_f) = (F_r(t_n), F_r(t_f))$ the inverse lies in (t_n, t_f) . To compute $F_r^{-1}(y)$, we start with boundaries $t_l = t_n$ and $t_r = t_f$ and gradually decrease the gap between the boundaries based on the comparison of $F_r(\frac{t_l+t_r}{2})$ with y . Importantly, such procedure is easy to parallelize across multiple inputs and multiple rays.

However, we cannot back-propagate through the binary search iterations and need a workaround to compute the gradient $\frac{\partial t}{\partial \theta}$ of $t(\theta) = F_r^{-1}(y, \theta)$. To do this, we follow (Figurnov et al., 2018) and compute differentials of the right and the left hand side of equation $y(\theta) = F_r(t, \theta)$

$$\frac{\partial y}{\partial \theta} d\theta = \frac{\partial F_r}{\partial t} \frac{\partial t}{\partial \theta} d\theta + \frac{\partial F_r}{\partial \theta} d\theta. \quad (27)$$

By the definition of $F_r(t, \theta)$ we have

$$\frac{\partial F_r}{\partial t} = (1 - F_r(t, \theta))\sigma_r(t, \theta), \quad (28)$$

$$\frac{\partial F_r}{\partial \theta} = (1 - F_r(t, \theta))\frac{\partial}{\partial \theta}\left(\int_{t_n}^t \sigma_r(s, \theta)ds\right). \quad (29)$$

We solve Eq. 27 for $\frac{\partial t}{\partial \theta}$ and substitute the partial derivatives using Eqs. 28 and 29 to obtain the final expression for the gradient

$$\frac{\partial t}{\partial \theta} = \frac{\frac{\partial y}{\partial \theta} - (1 - F_r(t, \theta))\frac{\partial}{\partial \theta}\int_{t_n}^t \sigma_r(s, \theta)ds}{(1 - F_r(t, \theta))\sigma_r(t, \theta)}. \quad (30)$$

In our implementation, we use automatic differentiation to compute $\partial y / \partial \theta$ and $\frac{\partial}{\partial \theta}\int_{t_n}^t \sigma(s)ds$ to combine the results as in Eq. 30.

B. Computational Efficiency of Approximations

In this section, we analyze our approximation method's computational efficiency and compare it with numerical approximation from Eq. 4. To illustrate it in a more practical setting, we determine time performance of the estimates relative to the batch processing time of a radiance field model. As an example, we picked a recent voxel-based radiance field model DVGO (Sun et al., 2021) that parameterizes density field as a voxel grid and combines voxel grid with a view-dependent neural network to obtain a hybrid parameterization of radiance.

Despite the toy nature of the experiment, we focus on a setting and hyperparameters commonly used in the rendering experiments. We take a batch of size 2048, draw 256 points along each of the corresponding rays and use them to calculate density σ . In the baseline setting, we then use the same points to calculate radiance c and estimate pixel colors with Eq. 4. In contrast to this pipeline, we propose to use calculated values of σ to make a piecewise-constant approximation of density, generate a varying number (32, 64, 128, 256) of Monte Carlo samples and use them to calculate stratified version the color

Table 7: Computational complexity of three stages of color estimation.

	Voxel Grid (σ)	Hybrid (c)	$E\hat{C}$
Baseline	0.00025s	0.02887s	0.00187s
Ours, 32	0.00025s	0.00419s	0.00369s
Ours, 64	0.00025s	0.00665s	0.00372s
Ours, 128	0.00025s	0.01334s	0.00381s
Ours, 256	0.00025s	0.02887s	0.00383s

estimate (Eq 10). We parameterize σ with a voxel grid and c with a hybrid architecture, used in DVGO, with the default parameters. In the Table 7 we report time measurements for each of the stages of color estimation: calculating density field in 256 points along each ray, calculating radiance field in the Monte Carlo samples (or in the same 256 points in case of baseline) and sampling combined with calculating the approximation given σ and c (just calculating the approximation in case of baseline). All calculations were made on NVIDIA GeForce RTX 3090 Ti GPU and include both forward and backward passes.

First of all, σ computation time is equal for all of the cases and has order of 10^{-4} seconds, negligible in comparison with other stages. In terms of calculating the approximation, both baseline and our method work proportionally to 10^{-3} seconds, but Monte Carlo estimate take 2.3 to 2.4 times more. Nevertheless, in the mentioned practical scenario this difference is not crucial, since computation of c , the heaviest part, takes up to 3×10^{-2} seconds. Even in the case of 256 radiance evaluations the difference in total computation time is less than 10%. This makes our method at least comparable with the baseline for architectures that can evaluate the density field faster than the radiance field. At the same time, our approach allows to explicitly control the number of radiance evaluations k , which allows to improve computational efficiency even further given suitable architectures.

C. Picking Fine Points in Differentiable Hierarchical Sampling

We considered two options for picking N_f points for fine network evaluation: either take N_f samples from the proposal distribution (first option), or take the union of N_p grid points that were used to construct the distribution and $N_f - N_p$ new samples from the proposal distribution (second option, originally used in NeRF). In Table 1, we reported the best result out of the two options, and Table 8 presents the results for both options. Our method worked best with the first option. The baseline performed better with the first option for (16, 32), (32, 64) configurations and with the second option for other configurations. Comparisons in Table 2 were done in ($N_p = 32, N_f = 64$) configuration with the first option. We picked this configuration for comparison as both methods performed best with the same option and produced better results than in ($N_p = 16, N_f = 32$) configuration. In the ablation study in Table 3, we also showed that the base model works worse with the second option in ($N_p = 32, N_f = 64$) configuration on average across other scenes of Blender dataset.

Table 8: Comparison of various hierarchical sampling configurations on the Lego scene of Blender dataset.

	Evaluations		NeRF			RVS		
	N_p	N_f	PSNR \uparrow	SSIM \uparrow	LPIPS	PSNR \uparrow	SSIM \uparrow	LPIPS
Union	16	32	25.81	0.890	0.150	27.18	0.903	0.145
No union	16	32	27.09	0.913	0.121	29.18	0.928	0.112
Union	32	64	29.61	0.939	0.084	30.34	0.942	0.088
No union	32	64	30.11	0.947	0.070	31.89	0.955	0.066
Union	64	128	32.14	0.958	0.053	31.63	0.952	0.068
No union	64	128	31.87	0.958	0.054	32.80	0.963	0.051
Union	64	192	32.69	0.962	0.048	32.46	0.960	0.056
No union	64	192	32.14	0.960	0.051	33.03	0.964	0.047

D. Visualizations

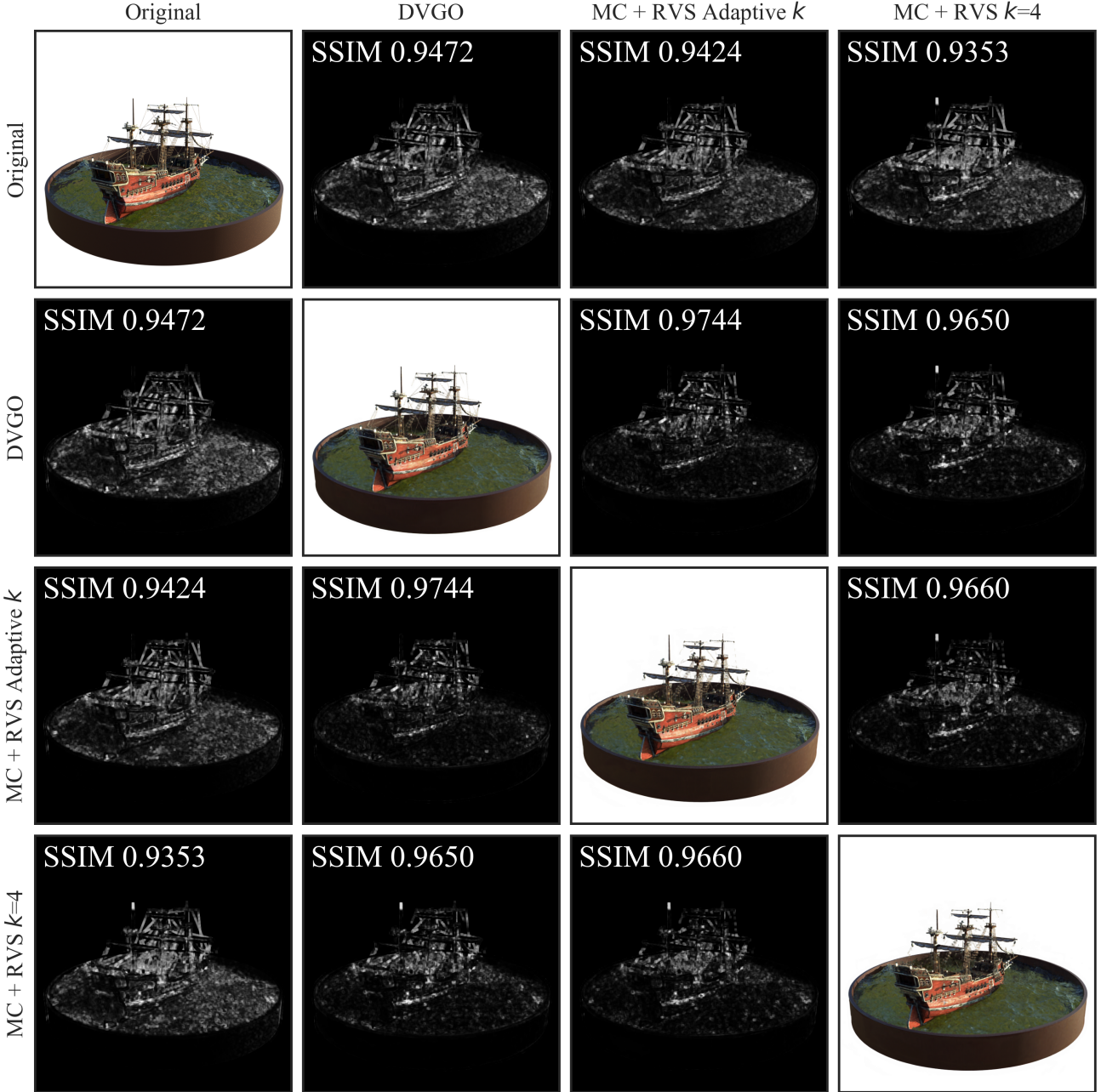


Figure 7: Qualitative comparison of scene reconstruction based on various training approaches. We visualize the default DVGO model along with two models trained using the reparameterized volume sampling algorithm (with the adaptive number of samples and $k = 4$ samples). In all three models, the novel view does not faithfully capture the water surface and fine ship details. Noticeably, the three models align in water surface reconstruction as opposed to the ship details. Perceptual quality of the details follows the numerical results.

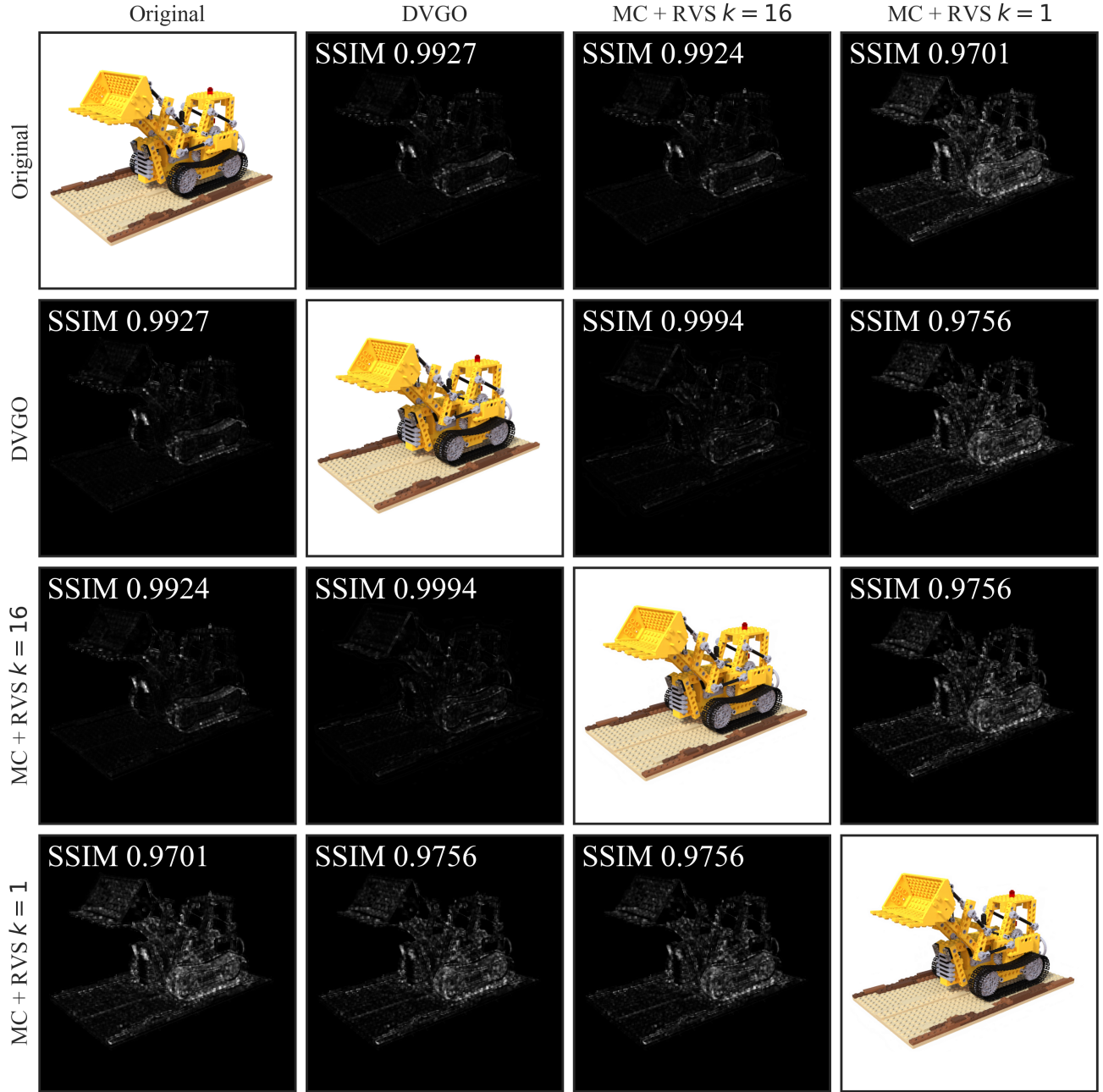


Figure 8: Comparison of novel views produced by different rendering algorithms. We trained a base DVGO model and rendered novel views using the default rendering algorithm and the proposed algorithm with $k = 1, 16$ samples. Except for a single-sample estimate, the rendered images on diagonal are barely distinguishable. Outside the diagonal, we visualize the difference with SSIM gradients and report SSIM between the images. The images produced with the default rendering algorithm and our algorithm with $k = 16$ differ the least, whereas the image with k samples has noticeable flaws near the track and edges.

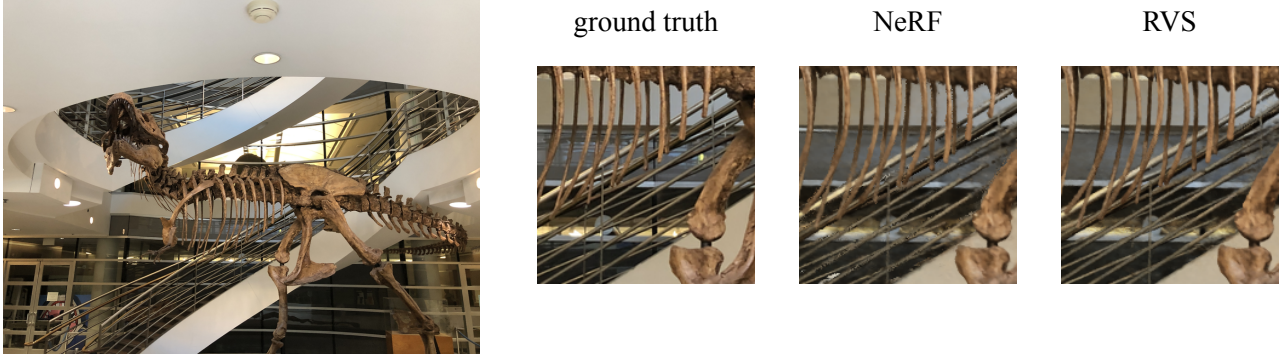


Figure 9: Comparison between renderings of test-set view on T-Rex scene (LLFF) for (32, 64) configuration. Artifacts can be seen on railings and bones in the baseline render, while reconstruction produced by our model lacks such artifacts.

E. Per-Scene Results

Table 9: Differentiable hierarchical sampling on Blender.

PSNR↑	Chair	Drums	Ficus	Hotdog	Lego	Materials	Mic	Ship	Avg
NeRF, ($N_p = 32, N_f = 64$)	31.33	23.89	28.26	35.44	30.11	28.65	31.46	26.76	29.49
RVS, ($N_p = 32, N_f = 64$)	31.99	24.60	29.27	36.18	31.89	29.31	31.84	27.19	30.26
SSIM↑	Chair	Drums	Ficus	Hotdog	Lego	Materials	Mic	Ship	Avg
NeRF, ($N_p = 32, N_f = 64$)	0.956	0.908	0.949	0.972	0.947	0.940	0.973	0.834	0.934
RVS, ($N_p = 32, N_f = 64$)	0.958	0.915	0.955	0.974	0.955	0.946	0.974	0.834	0.939
LPIPS↓	Chair	Drums	Ficus	Hotdog	Lego	Materials	Mic	Ship	Avg
NeRF, ($N_p = 32, N_f = 64$)	0.059	0.116	0.063	0.050	0.070	0.072	0.033	0.220	0.085
RVS, ($N_p = 32, N_f = 64$)	0.056	0.113	0.060	0.050	0.066	0.065	0.033	0.219	0.082

Table 10: Differentiable hierarchical sampling on LLFF.

PSNR↑	Room	Fern	Leaves	Fortress	Orchids	Flower	T-Rex	Horns	Avg
NeRF, ($N_p = 32, N_f = 64$)	31.22	24.79	20.81	31.00	20.32	27.41	25.89	26.64	26.01
RVS, ($N_p = 32, N_f = 64$)	31.87	24.89	20.89	31.11	20.27	27.40	26.48	26.98	26.24
SSIM↑	Room	Fern	Leaves	Fortress	Orchids	Flower	T-Rex	Horns	Avg
NeRF, ($N_p = 32, N_f = 64$)	0.938	0.771	0.678	0.875	0.630	0.822	0.858	0.798	0.796
RVS, ($N_p = 32, N_f = 64$)	0.942	0.773	0.681	0.878	0.630	0.823	0.869	0.795	0.799
LPIPS↓	Room	Fern	Leaves	Fortress	Orchids	Flower	T-Rex	Horns	Avg
NeRF, ($N_p = 32, N_f = 64$)	0.203	0.309	0.328	0.187	0.338	0.226	0.279	0.310	0.273
RVS, ($N_p = 32, N_f = 64$)	0.193	0.310	0.328	0.182	0.340	0.223	0.267	0.311	0.270

Table 11: DVGO with Monte Carlo estimates on Blender.

PSNR↑	Chair	Drums	Ficus	Hotdog	Lego	Materials	Mic	Ship	Avg
DVGO	34.07	25.40	32.59	36.75	34.64	29.58	33.14	29.02	31.90
MC + RVS, $k = 4$	33.79	25.16	31.81	36.22	33.35	28.32	33.03	27.87	31.19
MC + RVS, $k = 8$	33.49	25.16	31.30	36.26	33.34	28.64	32.87	27.99	31.13
MC + RVS, adaptive k	34.13	25.18	31.17	36.63	33.85	29.09	33.03	28.43	31.44
SSIM↑	Chair	Drums	Ficus	Hotdog	Lego	Materials	Mic	Ship	Avg
DVGO	0.976	0.929	0.977	0.980	0.976	0.950	0.983	0.877	0.956
MC + RVS, $k = 4$	0.976	0.927	0.975	0.979	0.971	0.938	0.982	0.857	0.951
MC + RVS, $k = 8$	0.973	0.927	0.972	0.979	0.970	0.942	0.981	0.861	0.951
MC + RVS, adaptive k	0.977	0.928	0.972	0.980	0.973	0.946	0.982	0.870	0.953
LPIPS↓	Chair	Drums	Ficus	Hotdog	Lego	Materials	Mic	Ship	Avg
DVGO	0.028	0.080	0.025	0.034	0.027	0.058	0.018	0.162	0.054
MC + RVS, $k = 4$	0.028	0.079	0.028	0.038	0.032	0.070	0.017	0.181	0.059
MC + RVS, $k = 8$	0.031	0.080	0.030	0.037	0.033	0.067	0.019	0.178	0.059
MC + RVS, adaptive k	0.027	0.081	0.031	0.034	0.031	0.062	0.019	0.165	0.056